Applied Surface Science 440 (2018) 61–72

Contents lists available at ScienceDirect

Applied Surface Science

journal homepage: www.elsevier.com/locate/apsusc

Full Length Article

Influence of Cu substitution on the structural ordering, photocatalytic activity and photoluminescence emission of $Ag_{3-2x}Cu_xPO_4$ powders

Wyllamanney da S. Pereira [a], Júlio C. Sczancoski [a,*], Yormary N.C. Calderon [b], Valmor R. Mastelaro [b], Gleice Botelho [c], Thales R. Machado [a], Edson R. Leite [a], Elson Longo [a]

[a] Universidade Federal de São Carlos (UFSCar), Departamento de Química, São Carlos, SP, Brazil
[b] Universidade de São Paulo (USP), Instituto de Física de São Carlos, São Carlos, SP, Brazil
[c] Universidade Federal do Tocantins (UFT), Química Ambiental, Gurupi, TO, Brazil

ARTICLE INFO

Article history:
Received 26 September 2017
Revised 19 December 2017
Accepted 21 December 2017
Available online 12 January 2018

Keywords:
Silver phosphate
Photocatalysis
Photoluminescence
Optical properties

ABSTRACT

Materials presenting high photocatalytic performance and interesting photoluminescence emissions are promising candidates for photodegradation of organic pollutants discharged into natural waters as well as for development of new electro-optical devices, respectively. In this study, $Ag_{3-2x}Cu_xPO_4$ (x = 0.00, 0.01, 0.02, 0.04 and 0.08) powders were synthesized by the precipitation method. The long- and short-range structural ordering was affected when the copper (Cu) content was increased in the lattice, as identified by X-ray diffraction patterns, Fourier transform infrared spectroscopy and Raman spectroscopy, respectively. The field emission scanning electron microscope and transmission electron microscope revealed a particle system composed of irregular spherical-like microcrystals. The presence of Cu as well as its real amount in the samples were confirmed by means of X-ray photoelectron spectroscopy and inductively coupled plasma-atomic emission spectrometry, respectively. On increasing Cu level, a slight variation was noted on the photocatalytic activity of $Ag_{3-2x}Cu_xPO_4$ powders for degradation of rhodamine B under visible light irradiation. A photodegradation mechanism was proposed in details. The photoluminescence emissions were explained by electronic transitions involving intermediary energy levels in the band gap. The origin these energy levels was related to defects caused by the substitution of Ag by Cu in the crystalline structure.

1. Introduction

Currently, the environmental problems have been considered one of the main concerns of the modern community, especially when it comes to water contamination. In this context, the organic dyes and pigments commonly used in the production line of some specific industries (textiles, leather, cosmetics, paper, etc.) have been discharged as untreated effluents into natural water resources or wastewater systems. These chemical substances are categorized as nature aggressor agents due to their high levels of toxicity and potential mutagenic and carcinogenic effects, resulting in serious risks to human health and severe impacts on ecosystems [1–4]. In particular, the textile industries are the largest consumer of organic dyes, presenting an annual production estimated at around 700,000 metric tonnes. However, 10–25% of these textile dyes are lost during the dyeing process, and 2–20% are incorrectly discharged as aqueous effluents without any treatment process [5,6]. A well-known industrial dye is Rhodamine B (RhB) (also commercially called Basic Violet 10), which is widely employed for the dyeing of cotton, weed, and clothes as well as in the preparation of ballpoint pen inks and stamp pad inks, and so on [7,8]. RhB is a non-volatile toxic substance and highly soluble in water, methanol and ethanol; hence, if swallowed by humans or animals, this dye causes serious irritations to the skin, eyes and respiratory system [9–11].

Due to increasing uncontrolled situation regarding the contamination of natural water sources, an international race has been motivated by scientists and environmentalists in order to find alternative solutions to prevent or minimize this grave global problem. Focused on this purpose, several treatment techniques based on biological, physico-chemical and photochemical processes have been developed over the years, for example, anaerobic/aerobic treatments [12], fungal discoloration [13], membrane separation [14], adsorption method [15], coagulation process [16], Fenton degradation [17], photocatalysis [18–20], and so on. Among all these different methods and from a practical point of view, the semiconductor-based photocatalytic degradation (PD) is an attractive route because of its important advantages, including low cost, easy to handle, reaction induced by visible or ultraviolet

* Corresponding author.
E-mail address: jcsfisica@gmail.com (J.C. Sczancoski).

https://doi.org/10.1016/j.apsusc.2017.12.202
0169-4332/

electromagnetic energies, minimal formation of secondary waste, no sludge disposal, mild temperature and pressure conditions [21,22]. The effectiveness of PD comes from its ability to produce highly reactive species, as hydroxyl (OH^*) and superoxide radicals ($O_2^{\prime}$), which are strong oxidizing agents responsible for degradation of different organic pollutants in aqueous medium [23–29].

In recent years, several researches have demonstrated that silver-containing materials exhibit an efficient photocatalytic performance [30–43], especially the silver phosphate (Ag_3PO_4) [44]. For example, Yi et al. [45] adopted for the first time the Ag_3PO_4 as active photocatalyst for specific purposes of water splitting and waste-water cleaning. This pioneering study provided the first formal scientific evidence on the strong photooxidative activity of this material to decompose organic contaminants. From this publication, other relevant studies have reported the importance of this semiconductor oxide as photocatalyst. Botelho et al. [46] correlated theoretical and experimental results to explain the morphological evolution and photocatalytic response of Ag_3PO_4 microcrystals composed of distinct particle shapes. Dong et al. [47] showed that the calcining process performed at different temperatures was able to improve the photooxidation property of this material by the creation of oxygen vacancies on the surface of the particles (increase of active sites). Li et al. [42] described a mechanism for the photocatalytic efficiency of Cu_2O/Ag_3PO_4 composites for the photodegradation of methylene blue (MB). According to these authors, photogenerated carriers can be easily separated, so that more holes can be found on the VB of Ag_3PO_4, while the additional electrons can enrich the CB of Cu_2O. These positive and negative charges promote the appearing of reactive species (hydroxyl and superoxide radicals) responsible for the efficiency in the PD process of MB. In a similar research, Lv et al. [43] explained that the high photocatalytic activity (PA) of $Cu/Ag/Ag_3PO_4$ heterostructures is arising from the effective separation of photogenerated carriers driven by the photoinduced potential difference generated at the metal-semiconductor heterojunction interface.

Another important property discovered in Ag_3PO_4 is photoluminescence (PL). Some studies previously published have demonstrated that this ceramic oxide exhibits broadband PL spectra with maximum emissions located in blue or green regions of the visible electromagnetic spectrum [48–54]. Thus, PL of this material can offer commercial opportunities and promising technological applications for the development of electronic components and equipments, for example, light-emitting diodes (traffic light signals, automotive lighting), lamps (illuminated advertising panels), lasers (dental repair, medical surgery).

In theory, a simple and efficient strategy to improve the PA, structural stability and PL property of Ag_3PO_4 is though the insertion of metal atoms in this crystalline lattice [55–57]. Therefore, in our present study, $Ag_{3-2x}Cu_xPO_4$ (x = 0.00, 0.01, 0.02, 0.04 and 0.08) powders were prepared by the simple precipitation method. The copper (Cu) atoms incorporated in this crystalline lattice induced a remarkable reduction in the average particle size as well as an improvement in structural stability of this photocatalyst during the first decomposition cycles of RhB solution under visible light irradiation at room temperature. Based on these experimental evidences, a photocatalytic reaction mechanism was proposed and discussed in detail. Moreover, the Cu content was able to change the final PL response of this phosphate matrix.

2. Materials and methods

2.1. Synthesis

$Ag_{3-2x}Cu_xPO_4$ powders were synthesized by the precipitation method at room temperature, as described in Ref. [48]. Silver nitrate ($AgNO_3$) (99.8%, Vetec), diammonium hydrogen phosphate ($(NH_4)_2HPO_4$) (98.6%, J. T. Baker) and copper nitrate trihydrate ($Cu(NO_3)_2{\cdot}3H_2O$) (98–102%, Synth) were chosen as chemical starting precursors. Initially, for the synthesis of $Ag_{3-2x}Cu_xPO_4$ with x = 0.00, 3 mmol of $AgNO_3$ and 1 mmol of $(NH_4)_2HPO_4$ were separately dissolved in beakers containing 50 mL of deionized water. Thereafter, $(NH_4)_2HPO_4$ solution was quickly added into the $AgNO_3$ solution, resulting in the instantaneous formation of $Ag_{3-2x}Cu_xPO_4$ (x = 0.00) precipitates (yellow coloration). This resulting mixture was maintained in constant stirring at room temperature for 10 min. Finally, the solid precipitates were separated from the liquid phase via centrifugation, washed with deionized water and acetone for six times, and dried in a lab oven at 60 °C for 12 h. On the other hand, for a stoichiometric composition of $Ag_{3-2x}Cu_xPO_4$ (x = 0.01, 0.02, 0.04 and 0.08), these powders were synthesized by using 1 mmol of $(NH_4)_2HPO_4$, 2.98, 2.96, 2.92 and 2.84 mmol of Ag^+ ions and 0.02, 0.04, 0.08, and 0.16 mmol of Cu^{2+} ions, respectively. In the preparation of these $Ag_{3-2x}Cu_xPO_4$ powders, both $Cu(NO_3)_2{\cdot}3H_2O$ and $AgNO_3$ precursors were dissolved together in 50 mL of deionized water. The following experimental steps adopted in this synthesis were the same for the preparation of $Ag_{3-2x}Cu_xPO_4$ (x = 0.00).

2.2. Characterizations

The structural analysis of $Ag_{3-2x}Cu_xPO_4$ powders was performed via X-ray diffraction (XRD) by using a D/Max-2500PC diffractometer (Rigaku, Japan) with CuKα radiation (λ = 0.154184 nm). Data were collected over 2θ ranging from 10° to 110° with a scanning scan rate and step size of 0.2°/min and 0.02°, respectively. X-ray photoelectron spectroscopy (XPS) was performed by using an ESCA + spectrometer (ScientaOmicron, Germany) with a high-performance hemispheric analyzer (EA 125) adjusted with a pass energy of 50 eV. A monochromatic Al$K\alpha$ (1486.6 eV) radiation was used as excitation source. Survey and high-resolution spectra for the main regions were recorded by using energy steps of 0.5 eV and 0.05 eV, respectively. The binding energies of all XPS spectra were calibrated in reference to C*1s* peak at 284.8 eV, corresponding to adventitious carbon. Charge neutralization was necessary during these measurements in order to stabilize uneven charges found on the surface of the samples and ensure a better peak shape. *CasaXPS* [58] software was used to analyze the XPS spectra, in which the core-level signals were individually fitted with Gaussian-Lorentzian functions and adopting a background subtraction according to Shirley method. The chemical composition of all samples was estimated by means of inductively coupled plasma-atomic emission spectrometry (ICP-AES) by using an iCAP 650 analyzer (Thermo Fisher Scientific, USA). Fourier transform infrared (FTIR) spectroscopy was performed by using a Bomem-Michelson MB-102 spectrophotometer. For these measurements, pellets were conformed in a composition of 1 wt.% of sample mixed with 99 wt.% of cesium iodide (99.9%, Aldrich). These measurements were recorded at a spectral resolution of 4 cm^{-1}, over wavenumbers ranging from 450 cm^{-1} to 4000 cm^{-1}. Raman spectroscopy were measured by using a T6400 spectrometer (Horiba Jobin-Yvon) coupled to a CCD Synapse detector, which is equipped with an argon-ion laser of 514 nm operated at 7 mW. These spectra were obtained over wavenumbers ranging from 50 cm^{-1} to 1200 cm^{-1}. The morphological aspects were analyzed by using a field-emission gun scanning electron microscopy (FEG-SEM) with a Supra 35-VP microscope (Carl Zeiss, Germany) operated at 5 kV. High-resolution transmission electron microscopy (HRTEM), selected area electron diffraction (SAED) and high angle annular dark-field scanning transmission electron microscopy (HAADF-STEM), and energy-dispersive X-ray spectroscopy (EDX) were performed with a TECNAI F20 microscope (Philips-FEI, Netherlands). Ultraviolet–visible (UV–vis) spectra were measured on a Varian

Spectrophotometer (Cary 5G, USA) operated in diffuse-reflection mode. PL spectra were performed at room temperature by using a Monospec 27 monochromator (Thermal Jarrel Ash, USA) coupled to a R446 photomultiplier (Hamamatsu Photonics, Japan). A krypton ion laser (Coherent Innova 200 K, USA) was used as excitation source (λ = 350 nm). The incident laser power on each sample was maintained at 15 mW.

2.3. Photocatalytic activities

The photocatalytic performances of $Ag_{3-2x}Cu_xPO_4$ powders under visible light irradiation were evaluated by using RhB in aqueous solution as representative pollutant. For these experiments, 50 mg of each sample was dispersed in 50 mL of dye solution (1×10^{-5} mol·L^{-1}) by means of an ultrasound bath (model 1510, Branson, USA) on a frequency of 42 kHz for 15 min. Before illumination, the suspension was magnetically stirred in the dark for 30 min to establish an adsorption-desorption equilibrium between dye and photocatalyst. The first aliquot (2 mL) was collected and considered as time zero. Afterwards, the photocatalytic system equipped with six lamps (Philips TL-D 15W/54-765, 15 W, visible wavelengths range from 380 nm to 680 nm, $\lambda_{max} \approx 440$ nm) illuminated the reaction medium, which was maintained at 20 °C by means of a thermostatic bath. Aliquots were collected at predetermined time intervals and immediately centrifuged (13,800 rpm for 20 min) in order to separate the precipitates from the RhB solution. Variations in the maximum absorbance band of RhB (λ_{max} = 554 nm) were monitored by using a V-660 UV–vis spectrophotometer (Jasco, Japan). The reusability and stability of $Ag_{3-2x}Cu_xPO_4$ powders (x = 0.00 and 0.01) as photocatalysts were investigated by three cycle runs.

2.4. Detection of reactive species

The experimental procedures used to identify the reactive species was similar to the photodegradation tests. In this case, different kinds of scavengers, such as isopropanol (ISO) (99.5%, Synth), p-benzoquinone (BQ) (99%, Merck), and di-ammonium oxalate monohydrate (AO) (99.5%-101%, Merck) were introduced into the RhB solution containing the photocatalyst. The molar concentrations adopted for these scavengers were all controlled at 1×10^{-3} mol·L^{-1} and 5×10^{-3} mol·L^{-1}, respectively.

3. Results and discussion

3.1. Long-range structural ordering

XRD patterns were employed to detect possible changes on crystallographic phases and/or degree of crystallization in $Ag_{3-2x}Cu_xPO_4$ powders in response to the addition of Cu in this structure. Initially, all detectable peaks were indexed to the body-centered cubic phase with space group $P\bar{4}3n$ (Inorganic Crystal Structure Database ICSD No. 14000) [59] (Fig. 1A). No secondary phases were observed in these diffractograms, suggesting that the Cu atoms were incorporated in the host lattice.

Another important feature detected in these diffractograms was the slight broadening of XRD peaks with the increase of Cu content in $Ag_{3-2x}Cu_xPO_4$ powders. This structural behavior can be easily identified by means of the most intense reflection peak from the (2 1 0) crystal plane (Fig. 1B). The full width at half maximum (FWHM) of this peak was used in the Debye-Scherrer equation [60] (Eq. S1 in Supplementary Material (SM)) to estimate the coherent crystalline domain size (D) of each sample (Table S1 in SM). As can be seen in this table, the broadening in XRD patterns as well as the decrease in D values are both attributed to the creation of defects (bulk, surface and interface), which are able to reduce the long-range structural ordering [61]. These defects are arising from a perturbation caused by the occupation of Cu species in sites commonly belonging to Ag in the body-centered cubic structure. Although both atoms have a coordination four, they have different ionic radius (0.73 Å for Cu^{2+} and 1.15 Å for Ag^{+}) [62].

The Rietveld refinement (RR) is a powerful tool to extract structural details from diffraction data of any crystalline solid. This approach is based on a least-squares fit between the theoretical and observed line profiles of XRD patterns [63]. In our study, the RR was employed to estimate the lattice parameters and unit cell volumes of $Ag_{3-2x}Cu_xPO_4$, mainly analyzing any influence induced by the substitution of Ag by Cu atoms. The structural refinements were performed by using the general structure analysis system (GSAS) software with the EXPGUI graphical interface [64]. The optimized parameters were scale factor, background with the Chebyschev polynomial of the first kind, shift lattice constants, profile half-width parameters (u, v, w), isotropic thermal parameters, lattice parameters, strain anisotropy factor, preferential orientation, and atomic functional positions. In addition, the peak profile function was modeled by using a convolution of the Thompson-Cox-Hastings pseudo-Voigt (pV-TCH) [65] with an asymmetry function, described by Finger, which accounts for the asymmetry resulting from axial divergence [66]. The theoretical diffraction pattern adopted in all refinements was taken from ICSD No. 14000 [59]. The RR plots and their respective structural results for each sample are displayed in Fig. S1 and Table S2 (SM).

In a first observation, there is a good fit between the theoretical and observed XRD patterns in all RR plots, which can be proven by the acceptable values of goodness of fit (χ^2) and R-factors (R_{Bragg}, R_{wp} and R_p). This information supports the confirmation in XRD patterns on the absence of secondary phases in $Ag_{3-2x}Cu_xPO_4$, independent of the Cu concentration. In addition, the obtained structural data are in perfect agreement with other studies previously published [46,48]. It was noted a slight difference in the lattice parameters and unit cell volume of $Ag_{3-2x}Cu_xPO_4$ (x = 0.08) in relation to other samples. This behavior can be due to the substitution process of Ag by Cu, leading to a rearrangement in the local geometry of [AgO_4], [CuO_4] and [PO_4] clusters.

The RR results inserted as input variables in the Visualization for Electronic and Structural Analysis (VESTA) software [67] allowed to model typical $Ag_{3-2x}Cu_xPO_4$ structures, in which both Ag and P atoms are coordinated to four oxygen (O) atoms (tetrahedral [AgO_4] and [PO_4] clusters) (Inset in Fig. S1A) [48,68,69]. In a schematic representation, the substitution of an Ag site by a Cu atom did not cause a collapse of the crystalline structure (Inset in Fig. S1B).

3.2. X-ray photoelectron spectroscopy (XPS)

The elemental identification and chemical state in the surface region of $Ag_{3-2x}Cu_xPO_4$ powders were investigated by XPS analysis. Typical XPS survey spectra of $Ag_{3-2x}Cu_xPO_4$ with x = 0.00 and 0.08 are illustrated in Fig. S2 (SM). The peak identification revealed the presence of Ag, P, Cu and O in the samples, except in $Ag_{3-2x}Cu_xPO_4$ with x = 0.00 and 0.01 (this is not shown here), in which the Cu peak was not detected. In this last case, as the Cu concentration is too low, it is impossible to affirm the existence of this element in this sample by XPS.

High-resolution spectra for Cu$2p$ levels (Fig. 2A) exhibited an improvement in the signal of the peaks with the continuous increase of Cu content. The noise is arising from the relatively small Cu amount as doping element. The two main Cu$2p$ peaks observed at 934.3 eV and 953.6 eV are ascribed to Cu$2p_{3/2}$ and Cu$2p_{1/2}$ levels related to Cu^{2+} ions, respectively. The broad peaks

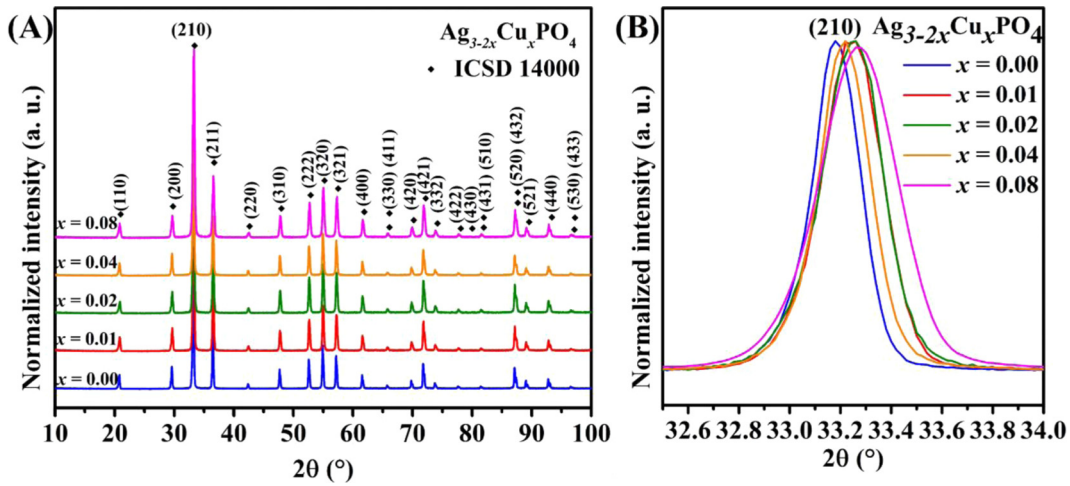

Fig. 1. (A) XRD patterns of $Ag_{3-2x}Cu_xPO_4$ (x = 0.00, 0.01, 0.02, 0.04 and 0.08); (B) magnified XRD patterns for highest intensity peak.

at 942.4 eV and 962.3 eV are typical satellite lines found in Cu2*p* spectra [70,71].

The existence of Ag on the surface of $Ag_{3-2x}Cu_xPO_4$ powders was investigated by means of Ag3*d* core levels. Ag $M_4N_{45}N_{45}$ and Ag $M_5N_{45}N_{45}$ Auger lines (Fig. S3 in SM) were used for the identification of Ag states [72]. The Auger line at 356.8 eV, in addition to the absence of small loss features in Ag3*d* spectra, confirmed the existence of Ag^+. The Ag3*d* peaks were fitted maintaining a 2:3 ratio between $Ag3d_{3/2}$ and $Ag3d_{5/2}$ levels corresponding to the spin-orbit splitting. For $Ag_{3-2x}Cu_xPO_4$ with x = 0.00, 0.01, 0.02 and 0.04, each of these Ag3*d* core levels were fitted into two components, i.e., at 367.40 eV and 368.39 eV for $Ag3d_{5/2}$, and at 373.46 eV and 374.42 eV for $Ag3d_{3/2}$, respectively (Fig. 2B and Fig. S4A-B in SM). According to the literature [73–79], the components observed at 368.39 eV and 374.42 eV are attributed to metallic silver (Ag^0). In this case, XPS analysis of Ag3*d* energy levels suggest that the Ag^0 species are randomly dispersed on the surface of these samples. It is important to emphasize that Ag^0 was not detected as secondary phase in the diffractograms because of the low detection limit imposed by the XRD technique (≈3% in a two-phase mixture) (Fig. 1A). In addition, the other two more intense components at 367.4 eV and 373.46 eV are due to Ag^+ belonging to $[AgO_4]$ clusters of Ag_3PO_4 phase.

On the other hand, the samples with high Cu concentration (x = 0.04 and 0.08) presented their $Ag3d_{5/2}$ and $Ag3d_{3/2}$ peaks well-deconvoluted into just one component, which is specific of a same oxidation state (Ag^+). This evidence indicates that the increase in the occupation of Ag sites by Cu atoms is able to create a high density of structural defects via modifications in bond lengths and distortions in bond angles (as oxygen vacancies) of both inter and intraclusters ($[AgO_4]$, $[CuO_4]$ and $[PO_4]$) [80]. Consequently, these defects have the ability to stabilize the cubic structure and prevent the reduction of Ag^0 on the surface.

The most notable changes in XPS spectra of $Ag_{3-2x}Cu_xPO_4$ powders were detected for the O1*s* core level. The curve fitting made for this spectrum revealed three spectral components, which pre-

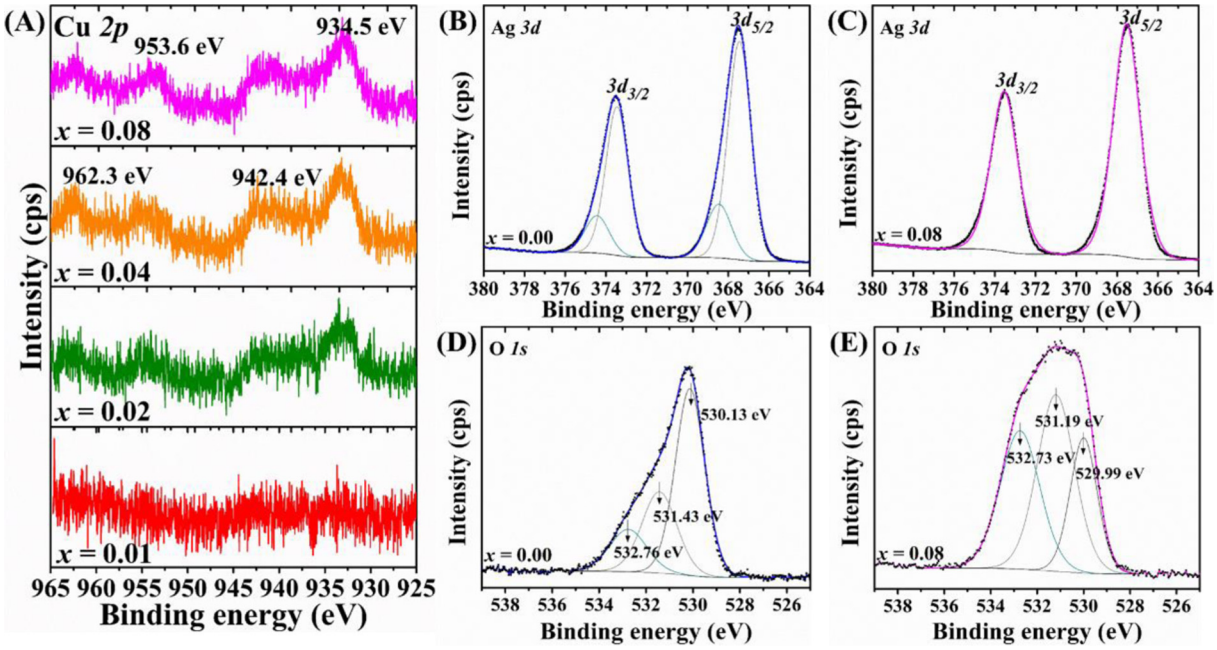

Fig. 2. Cu2*p* XPS spectra of (A) $Ag_{3-2x}Cu_xPO_4$ (x = 0.01, 0.02, 0.04 and 0.08). (B and C) Ag3*d* and (D–E) O1*p* XPS spectra of Ag_3PO_4 and $Ag_{3-2x}Cu_xPO_4$ (x = 0.08), respectively.

sented fluctuations on the binding energies, FWHM and peak shape from one sample to another (Fig. 2D–E and Fig. S4D–F in SM). In these figures, O*1s* component situated at around 530 eV is belonged to P—O bonds of [PO_4] clusters, while the other two found approximately from 531 eV to 532 eV are relative to O states arising from hydroxyl groups (H—O) chemisorbed on the surface [81]. The presence of P^{5+} in all samples was confirmed through binding energy of P*2p* core level, which exhibited a single peak centered at 132.38 eV [73,82] without changes in its profile (Fig. S5 in SM).

3.3. Inductively coupled plasma atomic emission spectroscopy (ICP-AES)

The high sensitivity and excellent detection capability presented by ICP-AES is a good alternative to estimate the real Cu amount found in $Ag_{3-2x}Cu_xPO_4$ powders. ICP-AES results in relation to the stoichiometric composition for the empirical Cu content (mol%) in all samples are summarized in Table 1.

The ICP-AES technique estimated that practically half of the Cu content was incorporated by the phosphate matrix in relation to the stoichiometric calculation. Despite this contrast, an important observation was the confirmation of Cu in $Ag_{3-2x}Cu_xPO_4$ (x = 0.01), which had not been detected by XPS spectra (Fig. 2A). Base on this evidence, we assume that the low Cu amount added in this sample is predominantly concentrated in the bulk than on the surface.

3.4. Short-range structural ordering

FTIR and Raman spectra were employed to identify the chemical nature and short-range structural ordering of $Ag_{3-2x}Cu_xPO_4$ powders, respectively. FTIR spectra obtained for our samples are shown in Fig. 3A, in which were noted typical vibrational bands related to [PO_4] clusters of Ag_3PO_4 phase. For example, O—P—O bending vibrations was detected at 537 cm^{-1}, P—O—P symmetric stretching vibrations at 672 cm^{-1}, P—O—P asymmetric stretching vibrations at 857 cm^{-1}, vibrations of isolated [PO_4] clusters at 985 cm^{-1}, asymmetric stretching vibrations of chain terminating of [PO_4] clusters at 1075 cm^{-1} and asymmetric stretching vibrations of [PO_4] clusters at 1377 cm^{-1} [46,83,84]. The other two absorption bands found at 3324 cm^{-1} and 1648 cm^{-1} are due to O—H stretching vibrations and H—O—H bending vibrations, both arising from residual water molecules adsorbed on the surface of the powders [84,85]. In practice, these FTIR spectra consolidate the supposition on the absence of any kind of impurity in these phosphates.

Raman spectra of $Ag_{3-2x}Cu_xPO_4$ powders are illustrated in Fig. 3B. According to theoretical calculations previously published [48], Ag_3PO_4 is characterized by a total of 18 Raman-active modes; however, our samples exhibited only seven of these respective modes. For example, the rotation and external vibrations were verified at 70 cm^{-1} (T_2) and 225 cm^{-1} (T_2), respectively. The two broad bands with low intensity located at around 411 cm^{-1} (E) and 553 cm^{-1} (T_2) are ascribed to symmetric and asymmetric bending vibrations of [PO_4] clusters, respectively. P—O—P symmetric and asymmetric stretching vibrations were detected at 914 cm^{-1} (A_1) and 955 cm^{-1} (T_2), respectively. The small band at 1007 cm^{-1} (T_2) is arising from terminal O bond vibrations in [PO_4] clusters [48,85–87]. The existence of Raman-active bands is a common nature of materials with short-range structural ordering [88]. In our Raman spectra, there is a gradual loss in the definition of these bands with the increase of Cu content in the $Ag_{3-2x}Cu_xPO_4$ lattice. Similarly to long-range structural ordering (XRD patterns in Fig. 1A), this phenomenon confirms that there is also a reduction in the local ordering because of the formation of structural defects caused by the incorporation of Cu species in Ag sites.

Table 1
ICP-AES results for Cu content in $Ag_{3-2x}Cu_xPO_4$ powders.

Theoretical (mol%)	Experimental (mol%)
0	0.00
1	0.50 ± 0.0004
2	0.94 ± 0.0005
4	1.99 ± 0.0006
8	4.38 ± 0.0009

3.5. Morphological aspects

FEG-SEM micrographs performed at low and high magnifications revealed that the $Ag_{3-2x}Cu_xPO_4$ powders, independent of the Cu fraction inserted in this host lattice, are composed of several irregular spherical-like microcrystals conformed in an aggregated assembly (Fig. 4). According to Botelho et al. [48], after the origin and interaction of the crystallites with the subsequent formation of primary particles, there is the predominance of particle-particle collision events. In a next stage, these particles are able to remain attached in a common crystallographic orientation (oriented attachment) accompanied by a growth process via coalescence, so that any misorientation in the solid-solid interface (imperfect oriented attachment) results in the creation of defects in this region [89,90]. Our micrographs also showed that the continuous addition of Cu (from x = 0.01 to 0.08) in the samples promoted a remarkable reduction in the average particle size (from 0.34 μm to 0.09 μm) as well as in a narrower particle size distribution (Fig. 5 and Fig. S6 in SM). Therefore, the substitution phenomenon with Cu has a key importance in the growth process of spherical-like microcrystals. As previously described, these Cu species influenced in the coherent crystalline domain size (Table S1 in SM), which play a crucial role on the genesis, growth and final arrangement of the particle system. In contrast, even in high concentrations, the presence Cu in the phosphate structure was not able to avoid the spontaneous appearing of irregular Ag^0 nanostructures on the surface of the microcrystals, when subject to the accelerated electron beam of FEG-SEM [48].

In general, a considerable number of published papers [48,56,76,84,91] has demonstrated the formation of these spherical-like microcrystals by means of other experimental routes. This evidence indicates that the final particle shape is controlled by the strong covalent character of P—O bonds (lattice former) in relation to the ionic character of Ag—O bonds (lattice modifier), even with the addition of other doping elements occupying the Ag sites.

TEM and HAADF-STEM analyses were performed in $Ag_{3-2x}Cu_xPO_4$ (x = 0.08) to investigate both morphological aspects and compositional homogeneity. This sample was chosen because of the high Cu content found in this crystalline lattice. In Fig. 6a, low magnification TEM micrograph proved that the spherical-like microparticles do not have a hollow structure. The SAED pattern corresponding to this image consisted of a series of concentric rings, which is a common feature of polycrystalline materials (Fig. 6b) [92]. This ring diffraction pattern was indexed to (2 0 0), (2 1 0), (3 1 0), and (3 2 1) crystalline planes of cubic Ag_3PO_4 phase, in good agreement with the XRD patterns reported in ICSD No. 14000 [59]. Fig. 6c shows a high magnification TEM image of a microcrystal, in which a HRTEM analysis was carried out on its edge (white square). HRTEM indicated that these microcrystals are composed of several nanoparticles, whose interplanar distance of a single particle was approximately 0.25 nm, corresponding to (2 1 1) plane of Ag_3PO_4 phase (Inset in Fig. 6c). The HAADF-STEM and EDX mapping showed a uniformity of all elements Ag, P and Cu in $Ag_{3-2x}Cu_xPO_4$ (x = 0.08) microcrystals (Fig. 6d). As pointed

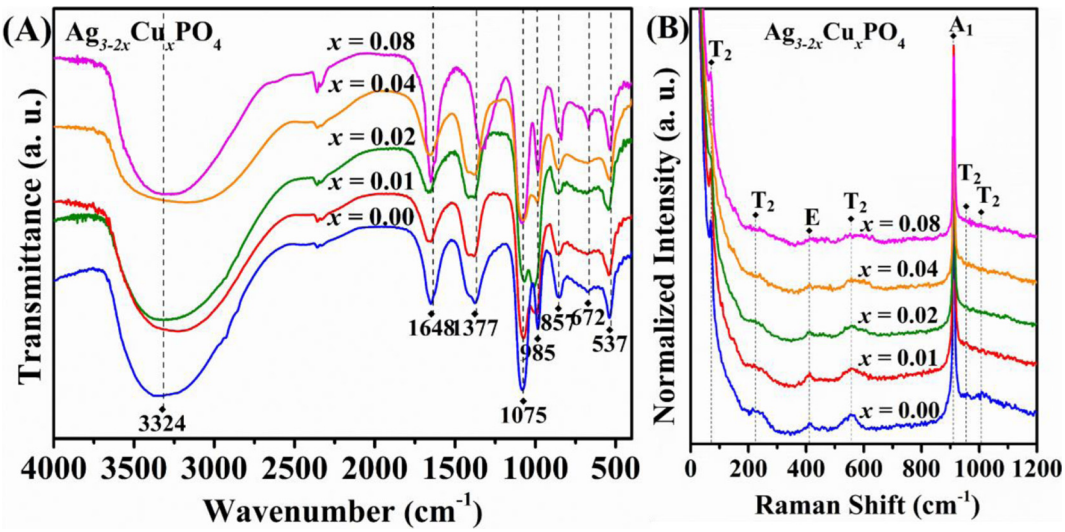

Fig. 3. (A) FTIR and (B) Raman spectra of $Ag_{3-2x}Cu_xPO_4$ (x = 0.00, 0.01, 0.02, 0.04 and 0.08), respectively.

out in XPS spectra (Fig. 2A) and ICP-AES (Table 1), this analysis also supports that the Cu atoms were incorporated in the host lattice, resulting in a good distribution of this element in both bulk and surface.

3.6. UV–vis absorption spectra and band gap energy

The band gap energy has an important impact on the selectivity and performance of the physical properties of semiconductors, especially for technological purposes focused on the fabrication of electro-optical devices, photovoltaic cells, photocatalysts and so on [93–95]. An alternative to manipulate the band structure of solids is to introduce new acceptor and/or donor levels in this forbidden region. Generally, these additional energy levels can be created manipulating the kind and concentration of dopant element in a particular crystalline lattice or inducing the formation of structural defects by means of an accurate control on the experimental parameters of a specific synthetic route [96]. In resume, the most common methodology employed to determine the band gap energy of semiconductors is based on UV–vis absorption spectra [97].

Typical UV–vis absorption spectra of $Ag_{3-2x}Cu_xPO_4$ powders are illustrated in Fig. S7 in SM, in which the E_{gap} values were estimated by using the Kubelka-Munk equation [98] for indirect allowed electronic transitions [68]. The E_{gap} results of all samples are displayed in Table 2. In this table, E_{gap} values exhibited slight differences when more Cu atoms substituted Ag in the crystalline structure. This phenomenon caused a symmetry break, as a response to changes provoked in bond lengths as well as distortions in atomic bonds, resulting in the appearing and redistributing of intermediary energy levels in the band gap.

3.7. Photocatalytic performance

The PA of $Ag_{3-2x}Cu_xPO_4$ powders was evaluated by monitoring the degradation of RhB under visible light irradiation. In this case, the behavior of the maximum absorption band of this organic dye (centered at 554 nm) was carefully checked with the time evolution by means of UV–vis absorption spectra (Fig. S8 in SM). In the absence of catalysts, the photolysis of RhB was practically negligible (at around 3.64%), after 24 min of exposure to visible light (Fig. 7). Adopting the PA of $Ag_{3-2x}Cu_xPO_4$ (x = 0.00) as a standard behavior, a slight loss in PD was noted in the other powders (x = 0.01, 0.02, 0.04 and 0.08) when more Cu was inserted (Fig. 7 and Fig. S8 in SM). Thus, the defects generated in the samples (bulk, surface and interface) by this element act as recombination centers, which have the ability to trap photo-generated electrons in a very short period of time [99]. Consequently, this mechanism can be considered one of the main agents responsible for minimizing the photocatalytic performance of $Ag_{3-2x}Cu_xPO_4$ powders. In addition, UV–vis spectra did not record any evidence on the formation of undesirable by-products during the photocatalytic tests.

The reaction kinetics responsible for PD of RhB, with and without the presence of catalysts, was well-described by a pseudo-first order rate law, as expressed by the following equation [100]:

$$-\left(\frac{C_n}{C_0}\right) = kt \tag{3.1}$$

where C_n is the concentration of RhB at time t, C_0 is the initial concentration of RhB, and k is the reaction rate constant.

The k values (min^{-1}) were graphically determined from the slope of $-\ln(C_n/C_0)$ as a function of the irradiation time (Fig. 7B). Theoretically, a low k reflects in a limited PA of the catalyst. All k values obtained for $Ag_{3-2x}Cu_xPO_4$ powders are listed in Table 3, which confirmed that high Cu amounts decrease the PA of these materials.

In principle, the photocatalytic property of any material is intrinsically related to some fundamental factors, such as structure, band gap energy, chemical composition, morphological aspects, surface area, among other [101,102]. From the surface point of view, the photocatalytic efficiency of Ag-based materials can be extremely influenced by the presence of Ag^0 on its surface [103–105]. According to the literature [105], the photogenerated electrons in the photocatalytic reaction are able to reduce part of Ag^+ ion found on the surface of Ag_3PO_4 to form Ag^0. These species act as recombination centers of photogenerated electron-hole (e'-$h^{\cdot}$) pairs, so that an excessive amount decrease the PA of the catalyst.

Based on this experimental observation, again the XRD and FEG-SEM analyzes were performed in $Ag_{3-2x}Cu_xPO_4$ powders after the photocatalysis tests to identify any evidence of Ag^0 on the surface of the microcrystals. Firstly, XRD patterns indicated the appearing of the (1 1 1) peak arising from Ag^0 (Fig. 8A). However, the intensity of this peak regularly decrease with the increase of Cu added as element substituent in $Ag_{3-2x}Cu_xPO_4$. In addition, typical FEG-SEM images of $Ag_{3-2x}Cu_xPO_4$ powders (x = 0.00 and 0.01)

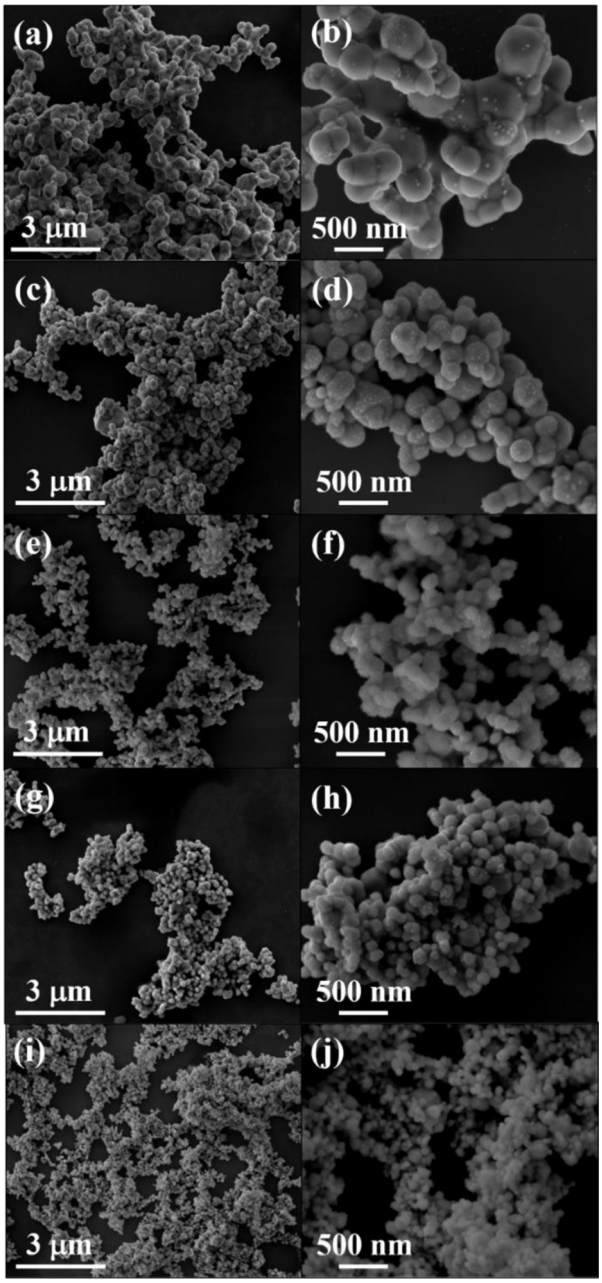

Fig. 4. Low and high-magnification FEG-SEM images of $Ag_{3-2x}Cu_xPO_4$ microcrystals with x = 0.00 (a, b), 0.01 (c, d), 0.02 (e, f), 0.04 (g, h) and 0.08 (i, j), respectively.

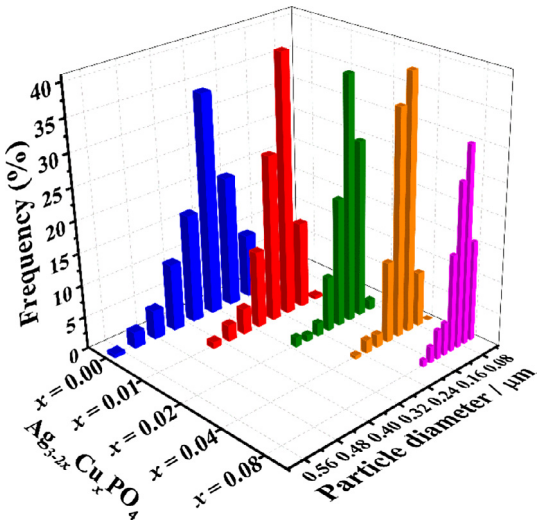

Fig. 5. Average particle size distribution of $Ag_{3-2x}Cu_xPO_4$ (x = 0.00, 0.01, 0.02, 0.04 and 0.08) microcrystals.

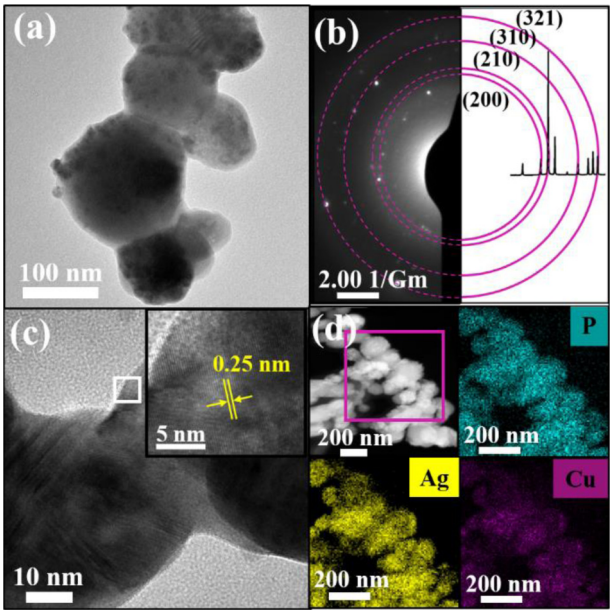

Fig. 6. $Ag_{3-2x}Cu_xPO_4$ (x = 0.08): (a) low magnification TEM image; (b) SAED pattern; (c) high-magnification TEM image and HRTEM analysis (Inset); (d) HAADF-STEM image and EDX mapping showing the elemental distribution of P, Ag, and Cu. The magenta square in HAADF-STEM image was the selected area for EDX analysis.

showed that the pure phase has a higher concentration of irregular Ag^0 nanostructures on its surface than the other sample containing the Cu substituent (white circles in Fig. 8B). Also, the digital photos (Insets in Fig. 8B) revealed a color change (from light yellow to dark yellow) in these powders after photocatalysis reactions, as a consequence of this growth phenomenon of Ag^0. In fact, both XRD and FEG-SEM measurements proved that the loss in PA of our samples was caused by the high concentration of structural defects originated by the substitution of Ag by Cu than due to the action of Ag^0 on the surface of the microcrystals. As previously explained, these defects stabilize the phosphate structure, inhibit the growth of Ag^0 nanostructures, and act as trapping centers of photogenerated e'-$h^{\cdot}$ pairs. It is important to highlight that the growth of Ag^0 nanostructures, after the photocatalysis reaction, causes also the formation of new structural defects. These defects promoted

Table 2
E_{gap} values of $Ag_{3-2x}Cu_xPO_4$ powders.

$Ag_{3-2x}Cu_xPO_4$	E_{gap} (eV)
x = 0.00	2.45
x = 0.01	2.46
x = 0.02	2.44
x = 0.04	2.46
x = 0.08	2.47

a rearrangement of intermediary energy levels in the band gap, increasing the E_{gap} values (Fig. S9 in SM).

Another photocatalytic test performed on the $Ag_{3-2x}Cu_xPO_4$ with x = 0.00 and 0.01 to verify the structural stability and photocatalytic performance was the recyclability. After three cycles of pho-

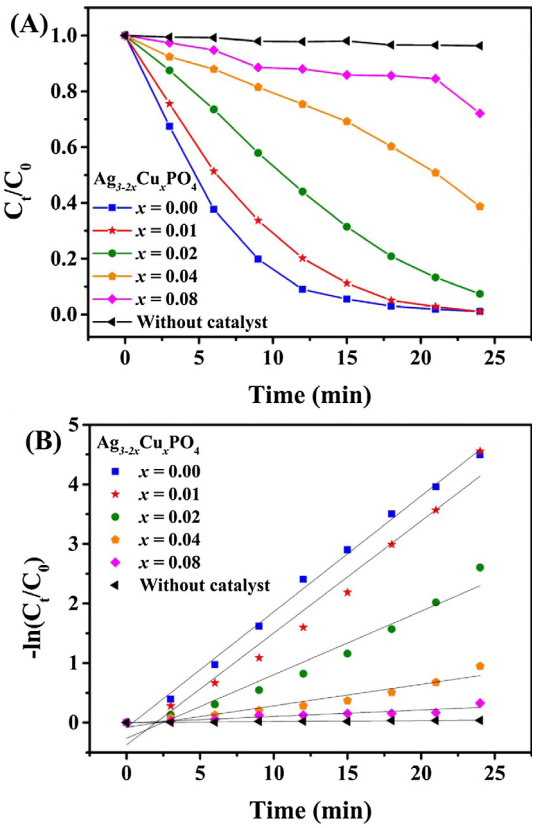

Fig. 7. (A) Photocatalytic activity and (B) pseudo-first order kinetics for photodegradation of RhB solution without and with $Ag_{3-2x}Cu_xPO_4$ (x = 0.00, 0.01, 0.02, 0.04 and 0.08), respectively.

Table 3
The k values of $Ag_{3-2x}Cu_xPO_4$ powders.

$Ag_{3-2x}Cu_xPO_4$	k (min^{-1})	R^{2*}	SD^{**}
x = 0.00	0.1945	0.9956	0.0046
x = 0.01	0.1880	0.9690	0.0119
x = 0.02	0.1067	0.9506	0.0086
x = 0.04	0.0361	0.9180	0.0038
x = 0.08	0.0109	0.8429	0.0016
Without catalyst	0.0016	0.9276	0.0001

* R^2 = correlation coefficient.
** SD = standard deviation.

todegradation, XRD patterns revealed the presence of diffraction peaks related to secondary phases (Ag^0 and silver peroxide (Ag_2O_2)) [106] in both powders (Fig. S10A-B in SM). However, the absence of the peak at around 41° related to Ag_2O_2 phase for $Ag_{3-2x}Cu_xPO_4$ (x = 0.01) indicated a slight structural stability of this material in relation to the pure phase. On the other hand, $Ag_{3-2x}Cu_xPO_4$ (x = 0.00) showed an effective PD of approximately 99% for RhB in all cycles, while the sample containing Cu atoms in its structure presented a substantial loss in PA until the end of the third cycle (56% in the PD of RhB) (Fig. S10C-D in SM). This behavior can also be observed in all recycle tests by means of UV–vis absorption spectra of the maximum absorption band of RhB (centered at 554 nm) as a function of the time evolution (Fig. S11 in SM). Moreover, FEG-SEM images of these powders exhibited a gradual degradation of the particle shapes with the increase in the number of cycles (Fig. S12 in SM). Beside of the appearing of asymmetrical Ag^0 nanostructures on the surface of the spherical-like microcrystals, the growth of some plate-like microcrystals since the second cycle was identified in this system (Inset in Fig. S12 (h)). In principle, these plate-like microcrystals can be arising from Ag_2O_2 phase [106]. In this case, these results reinforce the concept previously described that the insertion of Cu atoms in the lattice of this phosphate promotes a structural stability (mainly in the first cycle of photocatalysis), but with a consequent loss in PA because of several structural defects originated by the substitution process of Ag by Cu.

In order to identify the photocatalytic mechanism of $Ag_{3-2x}Cu_xPO_4$ with x = 0.00 and 0.01, some tests were conducted to ascertain the main reactive species responsible for photocatalytic process. Thus, ISO, BQ and AO were added to the photocatalytic system as scavengers for hydroxyl radicals (OH^*), superoxide radicals ($O_2^{\prime}$), and photogenerated holes ($h^{\cdot}$), respectively [91,107–109]. For the pure sample (Fig. 8C), BQ resulted in a weaker effect in the photocatalysis while the AO significantly inhibited this property. No change in the photocatalytic process was detected with the ISO. Therefore, $h^{\cdot}$ presented a key role in the PD of RhB than the $O_2^{\prime}$ and OH^*, respectively. On the other hand, when the $Ag_{3-2x}Cu_xPO_4$ (x = 0.01) was used as catalyst, both BQ and AO promoted a pronounced modification in PA in relation to ISO, indicating that both $h^{\cdot}$ and $O_2^{\prime}$ species contributed more strongly than the OH^* (Fig. 8D).

According to the literature [80,110], the existence of defects in the structure of a semiconductor facilitates the polarization process, leading to electronic transitions between ordered and disordered clusters with the formation of $e^{\prime}$-$h^{\cdot}$ pairs. In our study, a model based on complex clusters was proposed to explain the PA of $Ag_{3-2x}Cu_xPO_4$ powders for the photooxidation of RhB. During the photocatalytic reaction, $CuO_3V_o^{\cdot}]_d$, $[CuO_4]_o^{\cdot}$ and $[AgO_3V_o^{\cdot}]_d$ clusters react with the adsorbed water (H_2O) and/or RhB, while the ordered $[AgO_4]_o^{\prime}$ clusters interact with the adsorbed oxygen (O_2) species, as indicated from Eqs. (3.2)–(3.13).

$$RhB \xrightarrow{h\nu} RhB^* \tag{3.2}$$

$$[AgO_4]_o^x + [AgO_3V_o^x]_d \xrightarrow{h\nu} [AgO_4]_o^{\prime} + [AgO_3V_o^{\cdot}]_d \tag{3.3}$$

$$[AgO_4]_o^{\cdot} + [AgO_3V_o^{\cdot}]_d \xrightarrow{h\nu} [AgO_4]_o^{\prime} + [AgO_3V_o^{\cdot\cdot}]_d \tag{3.4}$$

$$[CuO_4]_o^{\cdot} + [CuO_3V_o^x]_d \xrightarrow{h\nu} [CuO_4]_o^x + [CuO_3V_o^{\cdot}]_d \tag{3.5}$$

$$[CuO_4]_o^{\prime} + [CuO_3V_o^{\cdot}]_d \xrightarrow{h\nu} [CuO_4]_o^{\cdot} + [CuO_3V_o^x]_d \tag{3.6}$$

$$[AgO_3V_o^{\cdot}]_d \cdots H_2O_{(ads)} \xrightarrow{h\nu} [AgO_3V_o^x]_d \cdots HO^*_{(ads)} + H^{\cdot} \tag{3.7}$$

$$[CuO_4]_o^{\cdot} \cdots H_2O_{(ads)} \xrightarrow{h\nu} [CuO_4]_o^x \cdots HO^*_{(ads)} + H^{\cdot} \tag{3.8}$$

$$[CuO_3V_o^{\cdot}]_d \cdots H_2O_{(ads)} \xrightarrow{h\nu} [CuO_3V_o^x]_d \cdots HO^*_{(ads)} + H^{\cdot} \tag{3.9}$$

$$[AgO_3V_o^{\cdot}]_d \cdots RhB_{(ads)} \xrightarrow{h\nu} [AgO_3V_o^x]_d \cdots RhB^*_{(ads)} \tag{3.10}$$

$$[CuO_3V_o^x]_d \cdots RhB_{(ads)} \xrightarrow{h\nu} [CuO_3V_o^x]_d \cdots RhB^*_{(ads)} \tag{3.11}$$

$$[CuO_4]_o^x \cdots RhB_{(ads)} \xrightarrow{h\nu} [CuO_4]_o^x \cdots RhB^{\cdot}_{(ads)} \tag{3.12}$$

$$[AgO_4]_o^{\prime} \cdots O_{2_{(ads)}} \xrightarrow{h\nu} [AgO_4]_o^x \cdots O^{\prime}_{2_{(ads)}} \tag{3.13}$$

where $H^{\cdot}$ and $O_2^{\prime}$ are species that can interact, generating the perhydroxyl radical ($HO_2^{\cdot}$), which contribute for PD of RhB. The subscripts (*ads*) in these equations indicate that are adsorbed species. The subscripts (*o*) and (*d*) significate ordered and disordered, respectively.

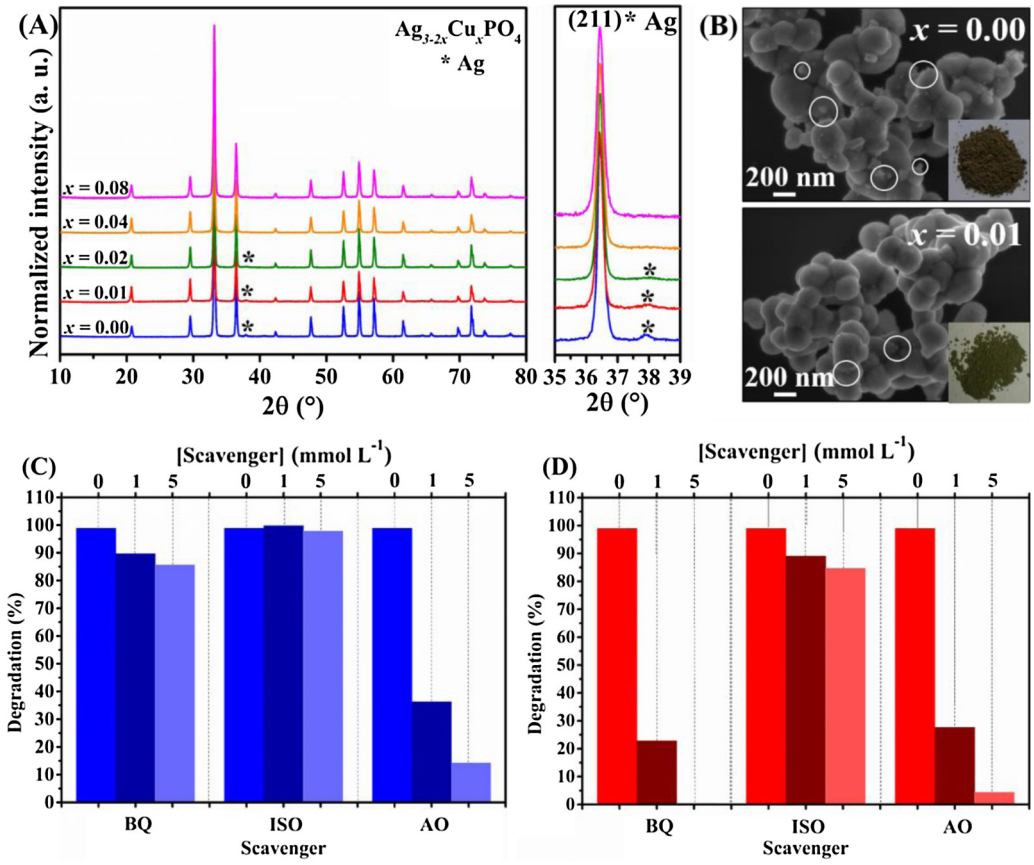

Fig. 8. (A) XRD patterns of $Ag_{3-2x}Cu_xPO_4$ (x = 0.00, 0.01, 0.02, 0.04 and 0.08) and magnified XRD patterns indicating the presence of the (1 1 1) peak (*) arising from Ag^0; (B) low magnification FEG-SEM images of $Ag_{3-2x}Cu_xPO_4$ (x = 0.00 and 0.01) microcrystals, demonstrating the regions with the growth of Ag^0 (white circles). Insets show the digital photos of the powders after photodegradation tests; Effects of different scavengers on the degradation of RhB by using $Ag_{3-2x}Cu_xPO_4$ with (C) x = 0.00 and (D) 0.01, respectively.

The superscripts (′) and (·) are ascribed to negatively and positively charged species in the lattice, respectively. The defects in the lattice, represented by oxygen vacancies (V_o), are found in different charge states in the disordered lattice, such as V_o^x (neutral states), $V_o^{\cdot}$ (single positive charged states – capture one electron) and $V_o^{\cdot\cdot}$ (double positive charge states – capture up to two electrons).

After several photooxidation cycles under visible light irradiation for 24 min, the PD of RhB by means of formed oxidant species (HO_2^*, O_2', and HO^*) occurs, according to Eq. (3.14).

$$RhB \xrightarrow{HO_2^* + O_2' + HO^*} CCO + CO_2 + H_2O \quad (3.14)$$

where CCO indicates the colorless organic compounds.

This proposed mechanism for PD of RhB by using $Ag_{3-2x}Cu_xPO_4$ powders as catalysts is shown in Fig. 9.

According to Eqs. (3.2)–(3.14), structural defects (for example, vacancy oxygens) are created because of variations in bond lengths and/or distortions in bond angles in [AgO_4], [CuO_4] and [PO_4] clusters, especially due to the substitution of Ag sites by Cu atoms into the lattice. These defects creates additional energy levels between VB and CB, causing the polarization of the crystalline structure via formation of e'-$h^{\cdot}$ pairs. Thus, the $[MO_4]^{\cdot}$ and/or $[MO_3V_o^{\cdot}]$ (M = Ag and/or Cu) clusters can effectively react with H_2O to form OH^*, improving the redox capacity for photodegradation of RhB under visible light irradiation. Moreover, the electrons in $[AgO_4]'$ clusters have enough energy to reduce O_2 to O_2', which is a strongly reactive specie in the photocatalytic process.

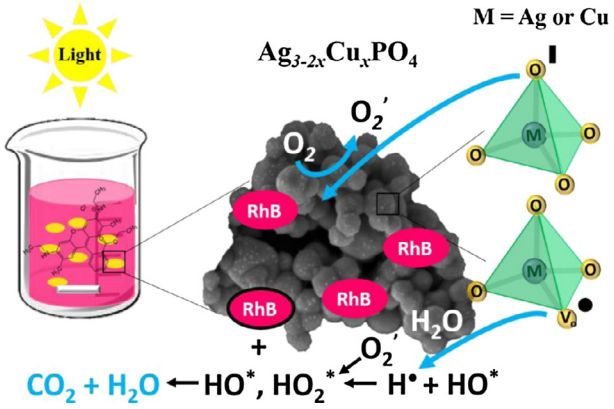

Fig. 9. Schematic representation of a photocatalytic mechanism for photodegradation of RhB by using $Ag_{3-2x}Cu_xPO_4$. The defects in [AgO_4] and/or [CuO_4] clusters in the lattice are able to produce highly reactive species in $Ag_{3-2x}Cu_xPO_4$ powders, which are responsible for photodegradation of RhB.

3.8. Photoluminescence spectra

The PL spectrum can be a useful approach to a qualitative understanding of the band structure of semiconductors. In general, the radiative recombination involving electronic transitions among different energy levels in the band gap yield different visible PL emissions (narrow or broadband). These energy levels are commonly classified in deep- and shallow-level defect states

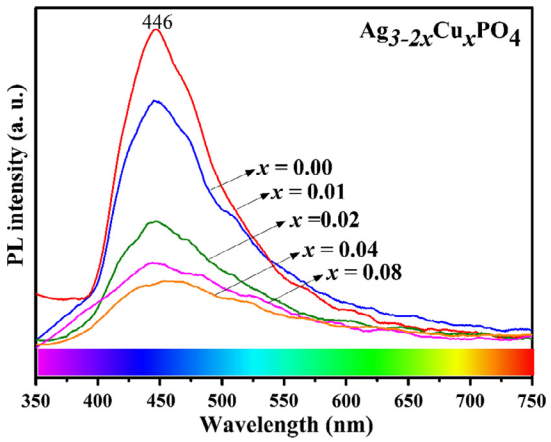

Fig. 10. PL spectra of $Ag_{3-2x}Cu_xPO_4$ (x = 0.00, 0.01, 0.02, 0.04 and 0.08).

[111,112]. The deep states are located almost at the center of the band gap and far from the band edges, which give rise to green, yellow, orange, and red emissions. The shallow states are located near the band edges, in which those closest to conduction band are responsible for violet and blue emissions [112,113].

Fig. 10 shows PL spectra performed at room temperature of $Ag_{3-2x}Cu_xPO_4$ powders by using an excitation wavelength of 350 nm. In a first observation, all spectra exhibited a broadband profile (common phenomenon of a variety of semiconductors), indicating the participation of numerous electronic transitions between energy levels [114–116]. Another point to be considered is that the excitation wavelength (~3.54 eV) is higher than the band gap found for our samples (from 2.16 eV to 2.30 eV); therefore, the contribution of band-to-band electronic transitions also have a significant impact on the final PL spectrum. In principle, the origin these intermediary energy levels are due to defects arising from modifications in bond lengths and/or distortions in bond angles (as oxygens vacancies) of both inter and intraclusters ($[AgO_4]$, $[CuO_4]$ and $[PO_4]$) because of the perturbation caused by the substitution process of Ag by Cu. As clearly observed in Fig. 10, there is a progressive reduction in PL intensity when the Cu amount was proportionally increased in the crystalline lattice, whose behavior reflects in an increase in the density of defects. Moreover, the maximum emission was observed at around 446 nm (blue light), indicating a majority participation of additional energy levels known as shallow-level defect states (near from the conduction band) arising from tetrahedral $[PO_4]$ clusters [46,48]. It is important to point out that extrinsic defects (cracks, pores, growth of Ag^0) caused by the synthesis conditions during the formation process of the microcrystals have a certain degree of contribution in other lower emissions that compose all broadband PL spectrum.

4. Conclusion

In summary, $Ag_{3-2x}Cu_xPO_4$ (x = 0.00, 0.01, 0.02, 0.04 and 0.08) powders were successfully synthesized by the precipitation method at room temperature. The sharp and well-defined diffraction peaks proved that all samples have a long-range structural ordering. On the other hand, the slight broadening of XRD peaks with the increase of Cu content was attributed to the creation of defects (bulk, surface and interface) caused by the atomic substitution of Ag by Cu in the host matrix. According to RR results, all powders crystallized in a body-centered cubic phase with space group $P\overline{4}3n$, without any evidence of secondary phases. XPS spectra and ICP-AES data showed that Cu atoms were well-incorporated in $Ag_{3-2x}Cu_xPO_4$. In addition, XPS spectra also detected the existence of Ag^0 on the surface of these powders. The short-range structural ordering was confirmed by means of FTIR and Raman spectra, which exhibited typical vibration modes arising from P—O bonds of $[PO_4]$ clusters. As revealed in FEG-SEM and TEM micrographs, all powders are composed of several irregular spherical-like microcrystals conformed in an aggregated profile. These micrographs also indicated that depending on the Cu concentration, there is a reduction in the average particle size of the microcrystals. UV–vis spectra suggested a profile governed by indirect allowed electronic transitions, which yielded different E_{gap} values for $Ag_{3-2x}Cu_xPO_4$. This phenomenon was mainly ascribed to the appearing of intermediary energy levels in the forbidden region, as a consequence of the creation of defects induced by the substitution process of Ag by Cu. When adopted as catalysts, the samples presented an effective PA for the degradation of RhB. The lowest photocatalytic efficiencies were noted in $Ag_{3-2x}Cu_xPO_4$ (x = 0.04 and 0.08), indicating a high density of defects in these structures. As these defects act as trapping centers of photogenerated e'-$h^{\cdot}$ pairs, there is a gradual loss in PA of these catalysts. The maximum PL emissions were verified in the blue region of the visible electromagnetic spectrum, suggesting a major participation of shallow-level defect states (near from the conduction band) arising from $[PO_4]$ clusters.

Acknowledgments

The authors are grateful to FAPESP (2015/11917-8; 2016/23663-3; 2013/07296-2; 2012/14004-5), CAPES (20131475) and CNPq (153299/2015-0; 147001/2013-7) for the financial support. Special thanks to Prof. Dr. Paulo S. Pizani, Prof. Dr. Maximo S. Li, Prof. Dr. Joaquim de Araújo Nóbrega, Dr. Alex Virgilio, Mr. Rorivaldo Camargo and Mrs. Madalena Tursi for their scientific and technical contributions.

Appendix A. Supplementary material

Supplementary data associated with this article can be found, in the online version, at https://doi.org/10.1016/j.apsusc.2017.12.202.

References

[1] S.P. Hinge et al., Combined removal of Rhodamine B and Rhodamine 6G from wastewater using novel treatment approaches based on ultrasonic and ultraviolet irradiations, Desalin. Water Treat. 57 (50) (2016) 23927–23939.
[2] A. Mohagheghian et al., Photocatalytic degradation of a textile dye by illuminated tungsten oxide nanopowder, J. Adv. Oxid. Technol. 18 (1) (2015) 61–68.
[3] N. Muhd Julkapli, S. Bagheri, S. Bee Abd Hamid, Recent advances in heterogeneous photocatalytic decolorization of synthetic dyes, Sci. World J. 2014 (2014).
[4] D.S. Kim, Y.S. Park, Photocatalytic decolorization of rhodamine B by immobilized TiO_2 onto silicone sealant, Chem. Eng. J. 116 (2) (2006) 133–137.
[5] A. Ajmal et al., Principles and mechanisms of photocatalytic dye degradation on TiO_2 based photocatalysts: a comparative overview, Rsc Adv. 4 (70) (2014) 37003–37026.
[6] K.M. Reza, A. Kurny, F. Gulshan, Parameters affecting the photocatalytic degradation of dyes using TiO_2: a review, Appl. Water Sci. 7 (4) (2017) 1569–1578.
[7] K.P. Mishra, P.R. Gogate, Intensification of degradation of Rhodamine B using hydrodynamic cavitation in the presence of additives, Sep. Purif. Technol. 75 (3) (2010) 385–391.
[8] Y.L. Pang, S. Bhatia, A.Z. Abdullah, Process behavior of TiO_2 nanotube-enhanced sonocatalytic degradation of Rhodamine B in aqueous solution, Sep. Purif. Technol. 77 (3) (2011) 331–338.
[9] M. Soylak et al., Determination of rhodamine B in soft drink, waste water and lipstick samples after solid phase extraction, Food Chem. Toxicol. 49 (8) (2011) 1796–1799.
[10] N. Barka et al., Factors influencing the photocatalytic degradation of Rhodamine B by TiO_2-coated non-woven paper, J. Photochem. Photobiol., A 195 (2) (2008) 346–351.
[11] R. Jain et al., Removal of the hazardous dye rhodamine B through photocatalytic and adsorption treatments, J. Environ. Manage. 85 (4) (2007) 956–964.

[12] S. Seshadri, P.L. Bishop, A.M. Agha, Anaerobic/aerobic treatment of selected azo dyes in wastewater, Waste Manage. (Oxford) 14 (2) (1994) 127–137.
[13] S.K. Sen et al., Fungal decolouration and degradation of azo dyes: a review, Fungal Biol. Rev. 30 (3) (2016) 112–133.
[14] K.M. Majewska-Nowak, Application of ceramic membranes for the separation of dye particles, Desalination 254 (1) (2010) 185–191.
[15] N.S.K.V. Ravi Vital Kandisa, Khasim Beebi Shaik, R. Gopinath, Dye Removal by adsorption: a review, J. Bioremed. Biodegr. 7 (6) (2016) 1–4.
[16] C.-L. Yang, J. McGarrahan, Electrochemical coagulation for textile effluent decolorization, J. Hazard. Mater. 127 (1) (2005) 40–47.
[17] J. Ma et al., Fenton degradation of organic compounds promoted by dyes under visible irradiation, Environ. Sci. Technol. 39 (15) (2005) 5810–5815.
[18] K. Hashimoto, H. Irie, A. Fujishima, TiO_2 photocatalysis: a historical overview and future prospects, Jpn. J. Appl. Phys. 44 (12R) (2005) 8269.
[19] J. Lv et al., Facile synthesis of Z-scheme graphitic-C_3N_4/Bi_2MoO_6 nanocomposite for enhanced visible photocatalytic properties, Appl. Surf. Sci. 358 (2015) 377–384.
[20] J. Lv et al., Multi-walled carbon nanotube supported CdS-DETA nanocomposite for efficient visible light photocatalysis, Mater. Chem. Phys. 186 (2017) 372–381.
[21] K. Kabra, R. Chaudhary, R.L. Sawhney, Treatment of hazardous organic and inorganic compounds through aqueous-phase photocatalysis: a review, Ind. Eng. Chem. Res. 43 (24) (2004) 7683–7696.
[22] P. Mahata et al., Photocatalytic degradation of dyes and organics with nanosized $GdCoO_3$, J. Phys. Chem. C 111 (4) (2007) 1665–1674.
[23] M.N. Chong et al., Recent developments in photocatalytic water treatment technology: a review, Water Res. 44 (10) (2010) 2997–3027.
[24] T.L. Hewer et al., Ag_3PO_4 sunlight-induced photocatalyst for degradation of phenol, RSC Adv. 4 (65) (2014) 34674–34680.
[25] D.T. Sawyer, J.S. Valentine, How super is superoxide?, Acc Chem. Res. 14 (12) (1981) 393–400.
[26] M. Hayyan, M.A. Hashim, I.M. AlNashef, Superoxide ion: generation and chemical implications, Chem. Rev. 116 (5) (2016) 3029–3085.
[27] J. Lv et al., Construction of organic–inorganic cadmium sulfide/diethylenetriamine hybrids for efficient photocatalytic hydrogen production, J. Colloid Interface Sci. 512 (2018) 77–85.
[28] J. Lv et al., Facile constructing novel 2D porous gC_3N_4/BiOBr hybrid with enhanced visible-light-driven photocatalytic activity, Sep. Purif. Technol. 178 (2017) 6–17.
[29] J. Lv et al., Controllable synthesis of inorganic-organic $Zn_{1-x}Cd_xS$-DETA solid solution nanoflowers and their enhanced visible-light photocatalytic hydrogen-production performance, Dalton Trans. 46 (34) (2017) 11335–11343.
[30] J. Song et al., Low temperature aqueous phase synthesis of silver/silver chloride plasmonic nanoparticles as visible light photocatalysts, Dalton Trans. 42 (38) (2013) 13897–13904.
[31] H. Tang et al., Shape-controllable synthesis and morphology-dependent photocatalytic properties of AgBr photocatalysts, J. Mater. Sci.: Mater. Electron. 27 (7) (2016) 6955–6963.
[32] X. Guo, D. Deng, Q. Tian, One pot controllable synthesis of AgCl nanocrystals with different morphology and their photocatalytic activity, Powder Technol. 308 (2017) 206–213.
[33] Z. Zheng et al., Visible-light-induced selective photocatalytic oxidation of benzylamine into imine over supported Ag/AgI photocatalysts, ChemCatChem 6 (5) (2014) 1210–1214.
[34] D. Xu et al., Photocatalytic activity of Ag_2MO_4 (M = Cr, Mo, W) photocatalysts, J. Mater. Chem. A 3 (40) (2015) 20153–20166.
[35] R. Roca et al., Facet-dependent photocatalytic and antibacterial properties of α-Ag_2WO_4 crystals: combining experimental data and theoretical insights, Catal. Sci. Technol. 5 (8) (2015) 4091–4107.
[36] C.A. Oliveira et al., Well-designed β-Ag_2MoO_4 crystals with photocatalytic and antibacterial activity, Mater. Des. 115 (2017) 73–81.
[37] Z. Wang et al., Plasmonic Ag_2MoO_4/AgBr/Ag composite: excellent photocatalytic performance and possible photocatalytic mechanism, Appl. Surf. Sci. 396 (2017) 791–798.
[38] Z. Wang et al., Facile preparation of two-dimensional Bi_2MoO_6@Ag_2MoO_4 core-shell composite with enhanced visible light photocatalytic activity, J. Alloys Compd. 729 (2017) 100–108.
[39] K. Dai et al., A facile fabrication of plasmonic gC_3N_4/Ag_2WO_4/Ag ternary heterojunction visible-light photocatalyst, Mater. Chem. Phys. 177 (2016) 529–537.
[40] Z. Wang et al., Facile synthesis of novel butterfly-like Ag_2MoO_4 nanosheets for visible-light driven photocatalysis, Mater. Lett. 196 (2017) 373–376.
[41] Z. Wang et al., Large scale and facile synthesis of novel Z-scheme Bi_2MoO_6/Ag_3PO_4 composite for enhanced visible light photocatalyst, Mater. Lett. 169 (2016) 250–253.
[42] Z. Li et al., Facile synthesis of novel octahedral Cu_2O/Ag_3PO_4 composite with enhanced visible light photocatalysis, Mater. Lett. 206 (2017) 48–51.
[43] J. Lv et al., Cu/Ag/Ag_3PO_4 ternary composite: a hybrid alloy-semiconductor heterojunction structure with visible light photocatalytic properties, J. Alloys Compd. 682 (2016) 778–784.
[44] K. Bad'urová et al., Photocatalytic activity of Ag_3PO_4 and some of its composites under non-filtered and UV-filtered solar-like radiation, Ceram. Int. 43 (4) (2017) 3706–3712.
[45] Z. Yi et al., An orthophosphate semiconductor with photooxidation properties under visible-light irradiation, Nat. Mater. 9 (7) (2010) 559.
[46] G. Botelho et al., Photoluminescence and photocatalytic properties of Ag_3PO_4 microcrystals: an experimental and theoretical investigation, ChemPlusChem 81 (2) (2016) 202–212.
[47] P. Dong et al., Origin of activity and stability enhancement for Ag_3PO_4 photocatalyst after calcination, Materials 9 (12) (2016) 968.
[48] G. Botelho et al., Experimental and theoretical study on the structure, optical properties, and growth of metallic silver nanostructures in Ag_3PO_4, J. Phys. Chem. C 119 (11) (2015) 6293–6306.
[49] P. Tan et al., Hierarchical flower-like $SnSe_2$ supported Ag_3PO_4 nanoparticles: towards visible light driven photocatalyst with enhanced performance, Appl. Catal. B 202 (2017) 326–334.
[50] C. Tang et al., Co_3O_4 nanoparticles decorated Ag_3PO_4 tetrapods as an efficient visible-light-driven heterojunction photocatalyst, Appl. Catal. B 181 (2016) 707–715.
[51] W.-C. Peng, X. Wang, X.-Y. Li, The synergetic effect of MoS_2 and graphene on Ag_3PO_4 for its ultra-enhanced photocatalytic activity in phenol degradation under visible light, Nanoscale 6 (14) (2014) 8311–8317.
[52] Y. Bu, Z. Chen, Role of polyaniline on the photocatalytic degradation and stability performance of the polyaniline/silver/silver phosphate composite under visible light, ACS Appl. Mater. Interfaces 6 (20) (2014) 17589–17598.
[53] D. Zhang, J. Wang, In situ photoactivated plasmonic Ag_3PO_4@silver as a stable catalyst with enhanced photocatalytic activity under visible light, Mater. Res. AHEAD (2017).
[54] J. Tang et al., A novel Ag_3AsO_4 visible-light-responsive photocatalyst: facile synthesis and exceptional photocatalytic performance, Chem. Commun. 49 (48) (2013) 5498–5500.
[55] H. Yu et al., Tunable photocatalytic selectivity and stability of Ba-doped Ag_3PO_4 hollow nanosheets, Chin. J. Catal. 36 (9) (2015) 1587–1595.
[56] Y.P. Xie, G.S. Wang, Visible light responsive porous Lanthanum-doped Ag_3PO_4 photocatalyst with high photocatalytic water oxidation activity, J. Colloid Interface Sci. 430 (2014) 1–5.
[57] S. Zhang, S. Zhang, L. Song, Super-high activity of Bi^{3+} doped Ag_3PO_4 and enhanced photocatalytic mechanism, Appl. Catal. B 152 (2014) 129–139.
[58] N. Fairley, CasaXPS: Spectrum Processing Software for XPS, AES and SIMS, Version 2.3. 15, Casa Software Ltd., Cheshire, 2009.
[59] R. Masse, I. Tordjman, A. Durif, Refinement of crystal-structure of silver monophosphate, Ag_3PO_4-existence of high-temperature form, Zeitschrift fur Kristallographie 144 (1–2) (1976) 76–81.
[60] P. Scherrer, Bestimmung der Grosse und der inneren Struktur von Kolloidteilchen mittels Rontgenstrahlen (1918), in: L.E. Alexander (Ed.), X-ray Diffraction Methods in Polymer Science, LE Alexander, 1969.
[61] P.H. Mayrhofer et al., Microstructural design of hard coatings, Prog. Mater. Sci. 51 (8) (2006) 1032–1114.
[62] R.D. Shannon, Revised effective ionic radii and systematic studies of interatomic distances in halides and chalcogenides, Acta Crystallogr. Sect. A: Cryst. Phys. Diffr. Theor. Gen. Crystallogr. 32 (5) (1976) 751–767.
[63] H. Rietveld, A profile refinement method for nuclear and magnetic structures, J. Appl. Crystallogr. 2 (2) (1969) 65–71.
[64] B.H. Toby, EXPGUI, a graphical user interface for GSAS, J. Appl. Crystallogr. 34 (2) (2001) 210–213.
[65] P. Thompson, D. Cox, J. Hastings, Rietveld refinement of Debye-Scherrer synchrotron X-ray data from Al_2O_3, J. Appl. Crystallogr. 20 (2) (1987) 79–83.
[66] L. Finger, D. Cox, A. Jephcoat, A correction for powder diffraction peak asymmetry due to axial divergence, J. Appl. Crystallogr. 27 (6) (1994) 892–900.
[67] K. Momma, F. Izumi, VESTA 3 for three-dimensional visualization of crystal, volumetric and morphology data, J. Appl. Crystallogr. 44 (6) (2011) 1272–1276.
[68] X. Ma et al., Origin of photocatalytic activation of silver orthophosphate from first-principles, J. Phys. Chem. C 115 (11) (2011) 4680–4687.
[69] Q. Liang et al., Hierarchical Ag_3PO_4 porous microcubes with enhanced photocatalytic properties synthesized with the assistance of trisodium citrate, CrystEngComm 14 (8) (2012) 2966–2973.
[70] J. Adhikary et al., Ag/CuO nanoparticles prepared from a novel trinuclear compound $[Cu(Imdz)_4(Ag(CN)_2)_2]$(Imdz = imidazole) by a pyrolysis display excellent antimicrobial activity, J. Mol. Struct. 1113 (2016) 9–17.
[71] C. Dong et al., Fabrication and functionalization of tunable nanoporous copper structures by hybrid laser deposition and chemical dealloying, Sci. Adv. Mater. 4 (2) (2012) 204–213.
[72] A. Machocki et al., Manganese–lanthanum oxides modified with silver for the catalytic combustion of methane, J. Catal. 227 (2) (2004) 282–296.
[73] J. Wan et al., In-situ synthesis of plasmonic Ag/Ag3PO4 tetrahedron with exposed 111 facets for high visible-light photocatalytic activity and stability, Ceram. Int. 41 (5) (2015) 6933–6940.
[74] H. Zhang et al., Tuning photoelectrochemical performances of Ag–TiO_2 nanocomposites via reduction/oxidation of Ag, Chem. Mater. 20 (20) (2008) 6543–6549.
[75] L. Cai et al., Highly effective and stable Ag_3PO_4–WO_3/MWCNTs photocatalysts for simultaneous Cr(VI) reduction and orange II degradation under visible light irradiation, Appl. Surf. Sci. 353 (2015) 939–948.
[76] W. Teng et al., In situ capture of active species and oxidation mechanism of RhB and MB dyes over sunlight-driven Ag/Ag_3PO_4 plasmonic nanocatalyst, Appl. Catal. B 125 (2012) 538–545.
[77] X. Xiao et al., A facile way to synthesize Ag@AgBr cubic cages with efficient visible-light-induced photocatalytic activity, Appl. Catal. B 163 (2015) 564–572.

[78] W. Zhao et al., A novel ternary plasmonic photocatalyst: ultrathin gC_3N_4 nanosheet hybrided by $Ag/AgVO_3$ nanoribbons with enhanced visible-light photocatalytic performance, Appl. Catal. B 165 (2015) 335–343.
[79] J. Lv et al., In situ controllable synthesis of novel surface plasmon resonance-enhanced $Ag_2WO_4/Ag/Bi_2MoO_6$ composite for enhanced and stable visible light photocatalyst, Appl. Surf. Sci. 391 (2017) 507–515.
[80] L. Cavalcante et al., Cluster coordination and photoluminescence properties of α-Ag_2WO_4 microcrystals, Inorg. Chem. 51 (20) (2012) 10675–10687.
[81] Y. Chang, M.L. Lye, H.C. Zeng, Large-scale synthesis of high-quality ultralong copper nanowires, Langmuir 21 (9) (2005) 3746–3748.
[82] J. Zhang et al., Facile and green synthesis of novel porous gC_3N_4/Ag_3PO_4 composite with enhanced visible light photocatalysis, Ceram. Int. 43 (1) (2017) 1522–1529.
[83] B. Choudhary, N. Singh, Properties of silver phosphate glass in the presence of nanosize cobalt and nickel oxides, J. Non-Cryst. Solids 440 (2016) 59–69.
[84] R. Dhanabal et al., Visible light driven degradation of methylene blue dye using Ag_3PO_4, J. Environ. Chem. Eng. 3 (3) (2015) 1872–1881.
[85] P. Dong et al., Ag_3PO_4/reduced graphite oxide sheets nanocomposites with highly enhanced visible light photocatalytic activity and stability, Appl. Catal. B 132 (2013) 45–53.
[86] B. Liu et al., Enhanced visible-light photocatalytic activities of Ag_3PO_4/MWCNT nanocomposites fabricated by facile in situ precipitation method, J. Alloys Compd. 596 (2014) 19–24.
[87] L. Liu et al., A stable $Ag_3PO_4@gC_3N_4$ hybrid core@shell composite with enhanced visible light photocatalytic degradation, Appl. Catal. B 183 (2016) 133–141.
[88] A. Gouveia et al., Experimental and theoretical investigations of electronic structure and photoluminescence properties of β-Ag_2MoO_4 microcrystals, Inorg. Chem. 53 (11) (2014) 5589–5599.
[89] R.L. Penn, J.F. Banfield, Oriented attachment and growth, twinning, polytypism, and formation of metastable phases: Insights from nanocrystalline TiO_2, Am. Mineral. 83 (9–10) (1998) 1077–1082.
[90] R.L. Penn, J.F. Banfield, Imperfect oriented attachment: dislocation generation in defect-free nanocrystals, Science 281 (5379) (1998) 969–971.
[91] C. Zhou et al., Partial oxidation controlled activity regeneration of used Ag_3PO_4 photocatalyst via removing the in situ surface metallic silver, Appl. Surf. Sci. 351 (2015) 33–39.
[92] M.A. Asadabad, M.J. Eskandari, Electron Diffraction, Modern Electron Microscopy in Physical and Life Sciences, InTech, 2016.
[93] N.H. Hussin et al., Study of structural, electronic and optical properties of lanthanum doped perovskite PZT using density functional theory, Appl. Mech. Mater. 864 (2017) 127–132.
[94] S. Dayal et al., Photovoltaic devices with a low band gap polymer and CdSe nanostructures exceeding 3% efficiency, Nano Lett 10 (1) (2009) 239–242.
[95] P.V. Kamat, Semiconductor surface chemistry as Holy Grail in photocatalysis and photovoltaics, Acc. Chem. Res. 50 (3) (2017) 527–531.
[96] P. Martin, Introduction to Surface Engineering and Functionally Engineered Materials, John Wiley & Sons, 2011.
[97] D.D. Mulmi, A. Dhakal, B.R. Shah, Effect of Annealing on optical properties of zinc oxide thin films prepared by homemade spin coater, Nepal J. Sci. Technol. 15 (2) (2015) 111–116.
[98] L. Tolvaj, K. Mitsui, D. Varga, Validity limits of Kubelka-Munk theory for DRIFT spectra of photodegraded solid wood, Wood Sci. Technol. 45 (1) (2011) 135–146.
[99] M. Ni et al., A review and recent developments in photocatalytic water-splitting using TiO_2 for hydrogen production, Renew. Sustain. Energy Rev. 11 (3) (2007) 401–425.
[100] H. Al-Ekabi et al., Kinetic studies in heterogeneous photocatalysis. 2. Titania-mediated degradation of 4-chlorophenol alone and in a three-component mixture of 4-chlorophenol, 2,4-dichlorophenol, and 2,4,5-trichlorophenol in air-equilibrated aqueous media, Langmuir 5 (1) (1989) 250–255.
[101] T. Tachikawa, S. Yamashita, T. Majima, Evidence for crystal-face-dependent TiO_2 photocatalysis from single-molecule imaging and kinetic analysis, J. Am. Chem. Soc. 133 (18) (2011) 7197–7204.
[102] Y. Bi et al., Facet effect of single-crystalline Ag_3PO_4 sub-microcrystals on photocatalytic properties, J. Am. Chem. Soc. 133 (17) (2011) 6490–6492.
[103] Yongqian Lei, G. Wang, Pengran Guo, Huacan Song, Silver phosphate based plasmonic photocatalyst: highly active visible-light-enhanced photocatalystic phoperty and photosensitized degragation of pollutants, Funct. Mater. Lett. 5 (2012) 1250047-1–1250047-5.
[104] H. Katsumata et al., Photocatalytic degradation of bisphenol A by Ag_3PO_4 under visible light, Catal. Commun. 34 (2013) 30–34.
[105] W. Wang et al., Visible-light photocatalytic activity and deactivation mechanism of Ag_3PO_4 spherical particles, Chem.–Asian J. 7 (8) (2012) 1902–1908.
[106] G.I. Waterhouse, J.B. Metson, G.A. Bowmaker, Synthesis, vibrational spectra and thermal stability of Ag_3O_4 and related Ag_7O_8X salts, Polyhedron 26 (13) (2007) 3310–3322.
[107] M. Ge, Photodegradation of rhodamine B and methyl orange by Ag_3PO_4 catalyst under visible light irradiation, Chin. J. Catal. 35 (8) (2014) 1410–1417.
[108] X. Wang et al., Removal of microcystins (-LR, -YR, -RR) by highly efficient photocatalyst Ag/Ag_3PO_4 under simulated solar light condition, Chem. Eng. J. 230 (2013) 172–179.
[109] J. Cao et al., Visible light photocatalytic activity enhancement and mechanism of $AgBr/Ag_3PO_4$ hybrids for degradation of methyl orange, J. Hazard. Mater. 217 (2012) 107–115.
[110] L. Cavalcante et al., Growth mechanism and photocatalytic properties of $SrWO_4$ microcrystals synthesized by injection of ions into a hot aqueous solution, Adv. Powder Technol. 24 (1) (2013) 344–353.
[111] M.D. McCluskey, E.E. Haller, Dopants and Defects in Semiconductors, CRC Press, 2012.
[112] S. Lee et al., Paired gap states in a semiconducting carbon nanotube: deep and shallow levels, Phys. Rev. Lett. 95 (16) (2005) 166402.
[113] S. Rout et al., Photoluminescence property of $Ba(Zr_{0.25}Ti_{0.75})O_3$ powders prepared by solid state reaction and polymeric precursor method, Phys. B: Condens. Matter 404 (20) (2009) 3341–3347.
[114] S. Eliziário et al., Morphology and photoluminescence of HfO_2 obtained by microwave-hydrothermal, Nanoscale Res. Lett. 4 (11) (2009) 1371.
[115] J. Sczancoski et al., Effect of different strontium precursors on the growth process and optical properties of $SrWO_4$ microcrystals, J. Mater. Sci. 50 (24) (2015) 8089–8103.
[116] W. da Silva Pereira et al., Effects of chemical substitution on the structural and optical properties of α-$Ag_{2-2x}Ni_xWO_4$ ($0 \leq x \leq 0.08$) solid solutions, PCCP 18 (31) (2016) 21966–21975.